Materials Advances

ROYAL SOCIETY OF CHEMISTRY

PAPER

View Article Online
View Journal | View Issue

Cite this: *Mater. Adv.*, 2024, **5**, 9684

Design and characterization of multi-component lamellar materials based on MWW-type zeolitic layers and metal oxide sub-domains†

Cristina Esteban, Alexandra Velty * and Urbano Díaz *

Received 18th September 2024,
Accepted 6th November 2024

DOI: 10.1039/d4ma00942h

rsc.li/materials-advances

The preparation of multi-component catalysts with tailored properties and high activity is essential for advancing sustainable catalytic processes and contributes to a healthy planet. In this study, we synthesised several families of multi-component materials by combining MWW-type zeolitic layers with MgAlCe oxide sub-domains at the nanometric scale, employing different approaches. Methods I and II involve the co-precipitation of MgAlCe LDH using various sources of Mg^{2+}, Ce^{4+} and Al^{3+} in the presence of MWW zeolites. Method III utilizes swelling and intercalation of MWW with pre-formed LDH phases. After calcination, multi-component materials with integrated zeolitic layers and MgAlCe oxides were obtained, revealing significant structural differences across the methods. Method II allowed the co-precipitation of MgAlCe LDH sub-domains and promoted strong interactions between these LDH sub-domains and the MWW zeolite structure, disrupting regular LDH stacking. This interaction affects the structural organisation and results in inconsistently and irregularly stacked LDH layers, as shown by XRD patterns. Moreover, the presence of strong interactions with the zeolitic framework led to modify the chemical environment of the MWW structure. The characterization study revealed that these materials possess accessible acidic, basic, and redox sites, underscoring their potential as multi-functional catalysts. The homogeneous distribution of active sites within the porous zeolitic network would facilitate cooperative interactions between active centres of the zeolite structure and metallic oxides, while the small particle size and high dispersion of MgAlCe oxides should improve both the accessibility to these active sites and their number. Collectively, these structural and chemical properties make these multi-functional and component materials promising candidates for heterogeneous catalytic applications contributing to sustainable development and supporting efforts for a healthier planet.

1. Introduction

Currently, the design and preparation of new multi-component catalysts with specific properties and high activity to carry out efficient chemical processes of high industrial interest, with a clear impact on our society, are decisive for obtaining high-added value products through economically and environmentally sustainable synthetic routes.[1,2] In this sense, the presence of different components in the same structure makes it possible to take advantage of the physicochemical characteristics of each element and, crucially, to generate new properties due to the synergies and cooperative effects established between all the components.[3,4]

The fabrication of multi-component materials can be achieved by simple physical mixing of different materials. However, their use as multi-functional catalysts in multi-step reaction processes faces adverse effects attributed to phase segregation detected in their morphology and internal porosity, which induce low selectivities and hinder mass transfer of reactants and products.[5,6] These drawbacks can be solved by establishing the appropriate interactions between the different components that make up a multifunctional material connected at the nanoscale by covalent, coordinative, ionic or weaker bonds, such as van der Waals and hydrogen bonds. These approaches make it possible to obtain materials with a homogeneous distribution and organisation of the different sub-domains and functionalities in their skeleton, sufficiently isolated and separated at molecular distances to ensure maximum reactivity and efficiency.[7]

A strategy to prepare such homogeneously organised multi-component materials in suitably connected sub-domains is based on a valuable property of lamellar materials, which is

---

Instituto de Tecnología Química, Universitat Politècnica de València, Agencia Estatal Consejo Superior de Investigaciones Científicas, Valencia 46022, Spain. E-mail: udiaz@itq.upv.es, avelty@itq.upv.es

† Electronic supplementary information (ESI) available. See DOI: **https://doi.org/10.1039/d4ma00942h**

the alteration of the order and spatial arrangement of their layers by modifying their morphology and textural properties using chemical, mechanical or physical methods.[8] Moreover, their composition can be tuned by the inclusion or deposition of different organic or inorganic components on their external surface or in the interlamellar space, providing new physicochemical properties, additional active sites and extra-functionalities to the designed materials.[9] New families of swollen, exfoliated or pillared materials with multiple applications in catalysis, adsorption–gas separation, detection, photoluminescence, conductivity or controlled release of active molecules can be obtained by means of these functionalising preparation routes.[10,11] Lamellar precursors, on the other hand, offer the possibility of isolating and separating their sheets in individual layers, as low-dimensional construction units, offering high accessibility and variety in their composition, enabling the generation of new materials.[12] Likewise, following these strategies, materials derived from graphene,[13] lamellar zeolites,[14] layered double hydroxides[15] or lamellar phosphonates[16] have been obtained from the modification of the individual layers that constitute them, either by the introduction of new components on their surface by the inclusion of other structural sub-domains in their interlamellar space or also by their morphological alteration when subjected to post-synthesis treatments.[17]

However, the use of these 2D subunits as a starting point for the *in situ* generation of other nanoscale structures, which will be formed on their external surface, localised and stabilised in their interlamellar space directly during the synthesis process, remains to be studied in depth.[18,19] This strategy would allow the generation of multicomponent materials formed by different sub-domains with different functionalities and characteristics that would be closely related in the same porous matrix.[20] This would facilitate the presence of different active sites homogeneously distributed in the support lattice, perfectly isolated, avoiding their mutual neutralisation and allowing them to act cooperatively, without losing the high accessibility and stability that characterise these lamellar inorganic materials.[21]

In this study, different materials have been prepared from individual MWW-type layers present in the lamellar precursor of 3D MCM-22-type zeolites.[22] Considering their silicoaluminate nature and using the appropriate synthesis conditions, it was possible to prepare *in situ* nanometric sub-domains of layered double hydroxides on the surface and inside the microporous half cavities and channels present in the individual MWW layers, favoured by the presence of aluminium tetrahedral units in the zeolitic structure.[23] Alternatively, multi-component materials were also prepared by combining MWW lamellar phases with previously synthesised layered double hydroxides, using swelling and exfoliation techniques.[24] In all cases, after a calcination process to remove the structure-directing agents located in the interlamellar space, 3D MWW-type zeolites were generated, which present on their inner surface, metal oxide units derived from layered double hydroxides homogeneously distributed at the nanometric scale, with no phase segregation or agglomeration of metal oxide sub-domains (Scheme 1). The second synthesis route, in which an external source of Al^{3+} was used, allowed successfully the co-precipitation of MgAlCe LDH sub-domains and promoted strong interactions between these LDH sub-domains and the MWW zeolite structure, disrupting regular LDH stacking. This interaction affects the structural organisation and results in inconsistently and irregularly stacked LDH layers, as shown by XRD patterns. Upon calcination, the LDH-derived oxides exhibit weak Brönsted basic sites due to surface OH groups, together with active Lewis basic sites from O^{2-}–Mg^{2+} acid–base pairs. The basicity of these sites varies with the coordination of the O^2-anions, and oxygen atoms at the corners have a higher basicity than those at the edges or faces due to their lower coordination. Thus, the formation of nanoscopic LDH sub-domains with a small particle size in calcined MWW-LDH samples will improve the overall basicity by increasing the number of low-coordination Lewis sites. In addition, the customisable zeolite composition allows the incorporation of metals (Al, Sn, Ti, and Zr) with tuneable Lewis acid centres suitable for various redox processes. In addition, the presence of ceria nanoparticles provides oxygen vacancies and Ce^{4+}/Ce^{3+} redox couples, which are of vital importance for redox reactions. Collectively, these structural and chemical properties make these multi-functional and component materials promising candidates for heterogeneous catalysis in reactions such as Meerwein–Ponndorf–Verley reductions,[25] Oppenauer or Baeyer–Villiger oxidations,[26] aldol condensations,[27] hydrogenations,[28] isomerizations,[29,30] dehydrations and water splitting processes,[31] among others.

2. Experimental section

2.1. Synthesis of MWW-MgCe multi-component materials

All samples were prepared using a two-step procedure. The zeolite precursor was synthesized according to the method previously reported in the literature.[32] In the second step, solution A was prepared by dispersing the zeolitic MWW precursor (0.5 g) in distilled water (300 mL) and then the desired amount of $Mg(NO_3)_2·6H_2O$ (1.1 g, Aldrich, purity 99%) and $Ce(NO_3)_3·6H_2O$ (0.1 g, Thermo Fisher, purity 99%) was added. Next, aqueous solution B formed by NaOH (7.2 g, Aldrich, purity 99%), $NaNO_3$ (1.9 g, Aldrich, purity 99%) and distilled water (200 mL) was added to solution A drop by drop to adjust and maintain the pH, with constant stirring at room temperature. Finally, the obtained slurry was aged at 100 °C for 24 h. Then, the precipitate was filtered, washed with distillate water and dried at 100 °C overnight. These precursors were calcined at 580 °C for 5 h in the presence of air to obtain the final materials. The obtained solids were labelled as MWW-MgCe-10, MWW-MgCe-12, MWW-MgCe-12.3 and MWW-MgCe-12.5, based on the pH that has been adjusted during the synthesis process.

2.2. Synthesis of MWW-LDH-*in situ* multi-component materials

For obtaining MWW-LDH-*in situ* materials, the synthesis of MWW precursors was carried out as previously described.[33]

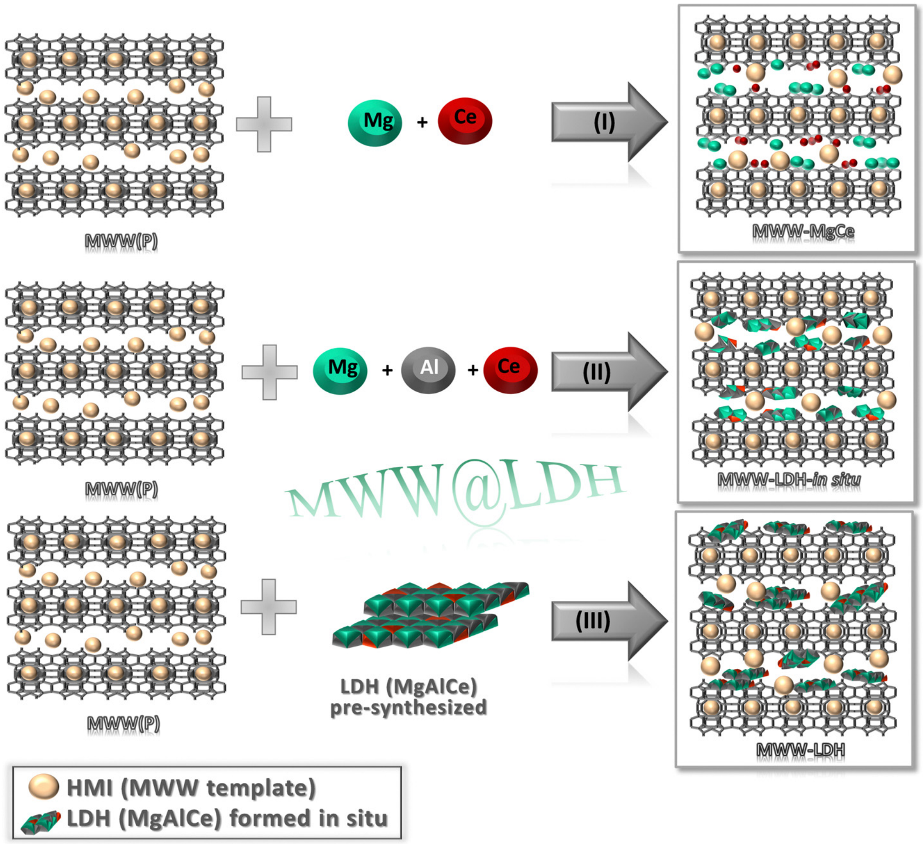

Scheme 1 Synthesis methodologies applied to prepare lamellar multi-component materials based on MWW-type zeolitic layers and MgCeAl oxide sub-domains combined at the nanometric scale.

An aqueous solution A (300 mL) consisting of $Mg(NO_3)_2{\cdot}6H_2O$ (0.39–0.64 g, Aldrich, purity 99%), $Al(NO_3)_3{\cdot}9H_2O$ (0.15–0.25 g, Thermo Fisher, purity 99%) and $Ce(NO_3)_3{\cdot}6H_2O$ (0.05–0.07 g, Thermo Fisher, purity 99%) was prepared. Then, the pH was adjusted with solution B (7.2 g of NaOH (Aldrich, purity 99%) and 1.9 g of $NaNO_3$ (Aldrich, purity 99%) in 200 mL of distilled water) to pH 12, with constant stirring at room temperature. After 10 min, the MWW zeolitic precursor (0.5 g) was added to the solution and stirring was maintained for 30 min. Finally, the obtained slurry was aged at 100 °C for 24 h. Then, the precipitate was filtered, washed with distilled water and dried at 100 °C overnight. These precursors were calcined at 580 °C for 5 h in the presence of air to obtain the final materials. The obtained solids were labelled as MWW-LDH(MgAlCe)-*in situ*-30, MWW-LDH(MgAlCe)-*in situ*-40 and MWW-LDH(MgAlCe)-*in situ*-50, based on the LDH content in the samples.

2.3. Synthesis of MWW-LDH multi-component materials

In the synthesis of MWW-LDH type materials, the zeolitic MWW precursor[25] and LDH (MgAlCe)[34] are previously synthesized, according to the literature. For the swelling process, 1 g of MCM-22(P) was dispersed in 6 g of H_2O milliQ and 20 g of the CTMAOH (25 wt%, 30% wt% exchanged OH^-/Br^-) and 6 g of TPAOH (40 wt%, 30 wt% exchanged OH^-/Br^-) were added. The obtaining slurry was heated at 80 °C with constant stirring under reflux for 16 h. Then, the solution was cooled at room temperature. The LDH (0.5 g) was added and the mixture was stirred for 24 h, followed by sonication of the slurry for 1 h. The solid was collected by centrifugation and dried at 100 °C overnight. This precursor was calcined at 580 °C for 5 h in the presence of air to obtain the final material, labelled as MWW-LDH(MgAlCe).

2.4. Characterization techniques

Powder X-ray diffraction (XRD) patterns of the different samples were recorded on a Philips X'PERT diffractometer equipped with a proportional detector and a secondary graphite monochromator. Data were collected stepwise over the angle range $2^\circ < 2q < 90^\circ$ using Cu Ka (l = 1,54178 Å) radiation.

The chemical composition of the sample was determined on a Spectra AA 10 Plus, Varian, after the dissolution of the solids in an aqueous solution of HNO_3/HCl/HF and heating in a microwave for 2 h.

Thermal gravimetric analysis and differential thermal analyses (TGA–DTA) were conducted in air streams using a Mettler Toledo TGA/SDTA 851E analyser.

Nitrogen adsorption isotherms were measured on a Micromeritics ASAP 2010 instrument using approximately 200 mg of the adsorbent placed in a sample holder that was immersed in a liquid circulation thermo-static bath for precise temperature control. Before each measurement, the sample was treated overnight at 673 K under a vacuum. The Brunauer–Emmett–Teller (BET) method was used to determine surface area and pore volume. Surface area was calculated from the data in the range from 0.04 to 0.2. The total pore volume was obtained from the amount of N_2 adsorbed at a relative pressure of 0.99. Finally, the external surface area and microporous volume were estimated using the *t*-plot method in the *t* range from 3.2 to 5.[35]

Transmission electron microscopy (TEM) was performed on a JEOL model JEM1400Flash with a STEM detector. For the analysis, a small amount of the sample was dispersed in dichloromethane. Then, a drop was placed on a copper grid and dried under a lamp for 2 h.

The UV-vis measurements were performed on a Cary 5 spectrometer equipped with a Diffuse Reflectance accessory.

Solid-state MAS-NMR spectra were recorded at room temperature under magic angle spinning (MAS) using AC-400 and AV-III HD-400 spectrometers. The single pulse ^{29}Si and ^{27}Al spectra were obtained at 79.5 MHz and 103.8 MHz, respectively, using a 7 mm Bruker BL-7 probe. ^{29}Si was referred to as tetramethylsilane, and ^{27}Al was referred to as aluminium nitrate.

TPR-H_2 profiles were obtained with a Micrometrics Autochem 2910 automated chemisorption analysis instrument. The samples were initially treated with 30 mL min^{-1} of Ar at 450 °C for 1 h. Then, the samples were reduced from 50 to 800 °C with a thermal ramp of 10 °C min^{-1} using an Ar: H_2 flow (10%H_2) of 50 mL min^{-1}.

The nature of acid sites was studied using TPD of preadsorbed and desorbed NH_3 on an Autochem II apparatus (Micromeritics). Approximately, 100 mg of samples were pretreated at 200 °C for 30 min under an O_2 flow (10 mL min^{-1}), then outgassed for 15 min under a He flow (100 mL min^{-1}) and cooled to 100 °C. Then, NH_3 adsorption was performed at 100 °C, using pulses of a known volume, until saturation of the solid. Finally, the sample was heated up to 800 °C (10 °C min^{-1}) under a He flow (100 mL min^{-1}). NH_3 desorption was analysed using a thermal conductivity detector and mass spectroscopy (OnmiStar, Pfeiffer).

3. Results and discussion

Various synthesis approaches were employed to prepare several families of multi-component materials based on the combination of MWW-type zeolitic layers and MgAlCe oxide subdomains at the nanometric scale. In all cases, prior preparation of lamellar silicoaluminate precursors, with MWW topology and Si/Al molar ratio of ∼15, was carried out to be used as support for *in situ* formed (II) or preformed (III) double-layered hydroxides (LDH), deposited onto the external surface of individual zeolitic layers. Additionally, these MWW-type precursors were not only used as support, but also as only source of aluminium for the *in situ* generation of external metal oxide phases (I), without the need to introduce additional aluminium sources during the process (Scheme 1). Through these synthesis methodologies, the aim is to prepare multi-component materials in which a favourable synergy is established between highly accessible zeolitic lamellar materials and MgAlCe oxide phases. These oxide phases should be homogeneously distributed as thin sub-structures on the surface and in the internal porous volume of the MWW-type zeolitic layers, combining the properties of both types of structural nanometric components.

3.1. Method (I): Synthesis of MWW-MgCe materials

The first synthesis methodology (I) was based on the formation of MgAlCe oxides formed on the surface of MWW-type zeolite layers, using aluminium from tetrahedral positions within the zeolite's structural framework as the aluminium source of the *in situ* formed metal oxide phases (MWW-MgCe). In this approach, only suitable magnesium and cerium salts were employed to form the MgAlCe hydrotalcite, with the purpose that aluminium would be directly contributed from the silicoaluminate units, which constitute the individual zeolite layers. In this case, the MCM-22 zeolite with a low Si/Al ratio (Si/Al = 25) was utilized, following literature references, to favour the effective formation of MgAlCe LDH phases. The results obtained through X-ray diffraction (XRD) revealed that the hydrotalcite phases were not satisfactorily obtained as sub-domains in the presence of MWW-type zeolites, as LDH diffraction bands were not observed in any case. Instead, oxide phases corresponding to Mg and MgAl oxyhydroxides ($Mg(OH)_2$ and $MgAlO_2$), as well as CeO_2, were detected, likely distributed on the surface of the zeolite sheets and in the interlayer space. The diffraction bands of these metal oxide sub-domains became more evident after the calcination process (Fig. 1).

This fact was confirmed by transmission electron microscopy (TEM), where the formation of CeO_2 nanoparticles evenly distributed within the structural framework of MCM-22 zeolites with an average size of ∼1.5 nm was clearly observed (Fig. 2). Using method (I), the co-precipitation of MgAlCe layered double hydroxides (LDHs) is primarily influenced and controlled by the low concentration of Al^{3+} available in the synthesis medium, which originates from the MWW-sheets. The absence of detectable LDH formation in XRD patterns suggests that the co-precipitation of LDH is directly competing with the adsorption of cations as Lewis acids onto the oxygen atoms of the MWW-sheets, acting as Lewis bases. The adsorption of $Mg(NO_3)_2$ and $Ce(NO_3)_3$ onto the oxygen atoms of MWW-type zeolitic layers can be understood through their Lewis acidity and following the trend $Ce^{4+} > Al^{3+} > Mg^{2+}$. It was concluded that the strong interaction between Ce^{4+} and Mg^{2+} and the zeolite surface, together with the very low concentration of Al^{3+} hinders the formation of LDH structures, promoting the formation of cerium oxide and Mg and MgAl oxyhydroxides. Chemical analysis results showed that the samples contained Mg in a ratio ranging from ∼2 wt% to ∼16 wt% and Ce around ∼6 wt%. Higher Mg content was observed when the pH increased during oxide phase formation during the preparation process, reaching more optimal conditions to form metal oxide sub-domains (Table 1). Thus, in cases where the synthesis pH was close to 12, which is more favourable for LDH-type phase formation and precipitation, a greater presence of Mg and MgAl oxyhydroxides, as well as CeO_2

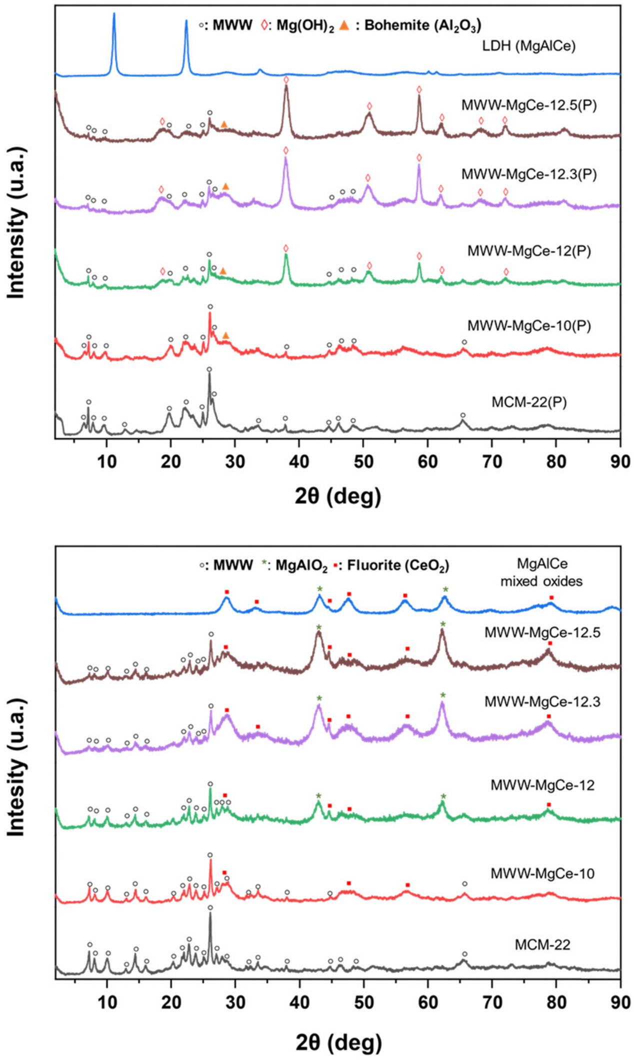

Fig. 1 XRD patterns of the multi-component MWW-MgCe materials obtained following synthesis method (I): (top) as-synthesized samples; (bottom) calcined samples.

nanoparticles, was observed, as confirmed by the higher contribution of these metallic phases detected in the obtained X-ray diffraction patterns (Fig. 1). It was also observed that under higher alkaline conditions used to generate metal oxide sub-domains, a partial desilication of the MWW-type counterpart occurred, resulting in a lower Si/Al molar ratio in the final obtained multi-component MWW-MgCe materials (Table 1). Thermogravimetric analysis (TGA) showed that the samples obtained at pH higher than 12 exhibited a more significant weight loss between 350 and 400 °C associated with the elimination of anionic counter-ions used for the formation of Mg, Al and Ce metallic oxyhydroxides (Fig. S1 and S2, ESI†). In all cases, a second weight loss at higher temperatures ($T >$ 500 °C) was also detected, attributed to dehydroxylation water generated by the condensation of external silanol groups present in the MWW layers present in the multicomponent materials. Moreover, the elimination of carbonates may have occurred in these elevated temperature ranges.

Furthermore, ^{29}Si and ^{27}Al NMR spectroscopy revealed that the structure of the MCM-22 zeolite remained unchanged after the oxide sub-domains formation process at different pH levels. The presence of Q^3 and Q^4 silicon atoms at chemical shifts characteristic of MWW-type zeolites was observed along with tetrahedral and octahedral aluminium. The latter is attributed to the presence of MgAl oxyhydroxide phases in the composition of the materials obtained through this synthetic approach (Fig. 3). In fact, a major contribution of octahedral aluminium was observed in the multi-component MWW-MgCe materials prepared at higher pHs, which favour the formation of oxide sub-domains. Additionally, ultraviolet-visible (UV-vis) spectroscopy emerges as a crucial tool for characterizing multi-component materials, such as those based on zeolite MWW-type sheets and metallic nanometric sub-domains of MgAl oxyhydroxides together with CeO$_2$ nanoparticles. Particularly, when studying the presence of CeO$_2$ nanoparticles in these materials, UV-vis spectroscopy offers crucial insights into the electronic transitions of cerium and its compounds. It is expected that UV-vis spectra reveal distinctive features, such as absorption shifts and peak intensities, thereby providing a detailed understanding of the incorporation and distribution of CeO$_2$ within the zeolite free porous volume and on the external surface of the MWW layers. These results showed that one prominent absorption peak for CeO$_2$ was detected around 330 nm for the different MWW-MgCe multi-component materials obtained at different pHs, before and after the calcination process, corresponding to the transitions involving Ce 4f electrons (Fig. S3, ESI†), characteristic of small CeO$_2$ nanoparticles homogeneously distributed in the zeolitic support.[36]

For these MWW-MgCe materials, the specific surface area and free pore volume were determined from nitrogen adsorption isotherms. It was observed that the microporous contribution of the solids decreased drastically with the increasing amount of metal oxide sub-domains formed on the lamellar surface and in the internal voids of the MWW-zeolitic structure at higher pHs (Table 2 and Fig. S4, ESI†). This result is consistent with the lower surface area and more compact structure of metallic oxides present in the multi-component MWW-MgCe materials compared with the more accessible textural properties of MWW zeolites. In addition, the possible blockage in part of the internal zeolitic microporous channels and semi-cavities, due to the presence of metal oxide sub-domains, should contribute to the decrease of the final specific surface area and free microporous volume of the MWW-MgCe multicomponent materials. The observed increase in the total volume of the samples when the presence of metallic oxide sub-domains was higher should be associated with a smaller crystal size characteristic of calcined hydrotalcite phases and the consequent interparticle volume generated between the oxide crystallites.

Several reducibilities could be identified for the MWW-MgCe materials because of the different natures of the transition metal cations and the various metallic oxide sub-domains present in the multi-component framework. Fig. 4 shows the H$_2$-TPR curves of the calcined MWW-MgCe samples. The reduction

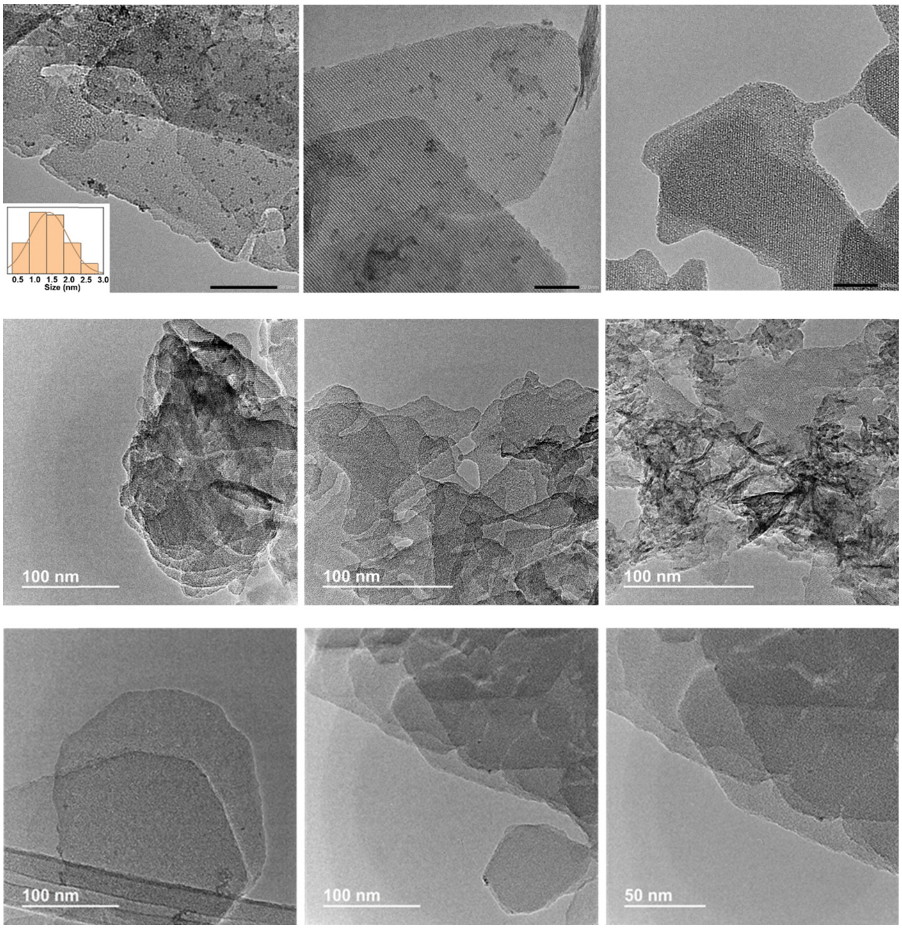

Fig. 2 TEM micrographs. (Top) Multi-component MWW-MgCe materials obtained following synthesis method (I) at different pHs to generate MgAlCe sub-domains. Inset with the histogram corresponding to sample MWW-MgCe-12, indicating dimensions of ceria nanoparticles. (Middle) Multi-component MWW-LHD-*in situ* materials obtained following synthesis method (II): (left) MWW-LDH(MgAlCe)-*in situ*-30, (center) MWW-LDH(MgAlCe)-*in situ*-40, (right) MWW-LDH(MgAlCe)-*in situ*-50. (Bottom) Multi-component MWW-LDH materials obtained following synthesis method (III) after the swelling and intercalation process.

temperature of CeO_2 was associated with signal at around 400 °C that was assigned to the reduction of oxides on the surface of zeolitic MWW layers.[37] This temperature is lower than for pure CeO_2, which would be ascribed to the ceria nanoparticles strongly interacting with MgAlO oxides and with MWW zeolitic layers, probably indicating a uniform dispersion of the metallic nanoparticles in the inorganic support. In addition, the H_2 reduction peak shifted to higher temperatures when the amount of cerium cations increased in the samples synthesized at higher pH levels, indicating that the CeO_2 nanoparticles agglomerated and reducibility weakened.

Furthermore, a temperature programmed desorption (TPD) ammonia study for the characterization of the acidity of the multi-component MWW-MgCe materials allowed to estimate the presence of acid sites located in the formed MWW-MgCe materials due to the presence of tetrahedral aluminium from individual zeolitic layers, and CeO_2 nanoparticles generated after the calcination process. The results showed that the solids with the highest amount of ceria nanoparticles, obtained at higher synthesis pHs, presented a remarkable ammonia desorption band in the temperature range of 300–350 °C. This band is attributed to the presence of acid ceria species in the multicomponent materials, a signal also observed in the pure phase of hydrotalcite MgAlCe.[38] This desorption band was practically indistinguishable in the sample obtained at a lower pH (MWW-MgCe-12), wherein the oxide sub-domain was formed in a small amount (Fig. 5). In fact, the desorption data reflect that the sample obtained at a pH of around 12.5 desorbed 136 $cm^3\ g^{-1}$ of ammonia, *i.e.* approximately four times more than that synthesized at lower pHs (Table S1, ESI†). On the other hand, the ammonia desorption bands detected at $\sim$200 °C and $\sim$400 °C, attributed to the acid sites from the MWW-type matrix, were also present in all multi-component MWW-MgCe materials confirming the coexistence of both sub-domains, *i.e.* zeolitic and derived metal oxide phases. In particular, the desorption band with lower intensity, observed at $\sim$200 °C, was probably due to the slight contribution of weak acid sites assigned to ammonia molecules interacting with surface silanol groups present on the surface of MWW zeolitic layers, and the desorption band at $\sim$400 °C was

Table 1 Chemical analysis (%wt and molar ratios) of multi-component MWW-MgCe, MWW-LHD-*in situ* and MWW-LHD materials obtained following synthesis methods (I), (II) and (III), respectively

Sample	%Si	%Al	%Mg	%Ce	Si/Al theor	Si/Al exp	Al/(Mg + Al + Ce) Theor[a]	Al/(Mg + Al + Ce) Exp[a]
MWW-MgCe materials								
MWW-MgCe-10	25.6	2.4	2.1	6.0	15	10.3	0.1	0.4
MWW-MgCe-12	20.5	1.8	15.7	5.1	15	11.1	0.1	0.1
MWW-MgCe-12.3	13.5	1.8	16.3	5.3	15	7.2	0.1	0.1
MWW-MgCe-12.5	14.0	1.7	11.9	6.0	15	6.3	0.1	0.1
MWW-LHD-*in situ* materials								
MWW-LDH(MgAlCe) *in situ*-30	21.1	3.3	6.4	2.2	9	6.1	0.19	0.16
MWW-LDH(MgAlCe) *in situ*-40	17.3	5.5	11.6	3.3	8	3.0	0.20	0.23
MWW-LDH(MgAlCe) *in situ*-50	14.7	5.7	12.9	14.7	7	2.5	0.19	0.22
MWW-LHD materials								
MWW-LDH(MgAlCe)	12.3	3.0	7.1	2.3	15	11	0.21	0.20

[a] In the case of MWW-LDH-*in situ* and MWW-LDH materials, it is considered that the Si/Al molar ratio of the MWW support is 11, based on the chemical analysis results obtained for this material.

associated with the presence of Brönsted acid sites from tetrahedral aluminium.[39]

3.2. Method (II): Synthesis of MWW-LDH-*in situ* materials

Considering that it was difficult to generate well identified MgAlCe hydrotalcite phases through the preparation method (I) discussed above, a second approach (II) was explored. In this case, external aluminium, magnesium, and cerium sources in the presence of MWW-type zeolites, previously prepared, were employed in the appropriate proportions in order to establish the most favourable conditions for the *in situ* formation of LDH-like phases deposited on/in the zeolitic structure (MWW-LDH-*in situ*) (Scheme 1). Using this procedure, a sufficient amount of aluminium necessary for the effective formation of MgAlCe hydrotalcite would be externally provided. Furthermore, the control of the alkaline conditions during the *in situ* formation of LDH would facilitate the optimal formation and precipitation of LDH phases cohabitating together with the MWW zeolitic counterpart. Following this procedure, increasing amounts of external Mg, Al and Ce sources were used with the objective to obtain MWW-LDH-*in situ* multi-component materials with a higher presence of the hydrotalcite phase (from 30 to 50 wt%, theoretically). The results obtained by X-ray diffraction showed that some of the characteristic diffraction bands of LDH-like materials appeared in the XRD patterns of the as-synthesized samples. In particular, the diffraction bands located at $\sim 33^\circ$ and $\sim 62^\circ$ 2θ were clearly observed, indicative of the formation of MgAlCe hydrotalcite phase. The other bands were masked by the diffraction bands associated with the MWW zeolitic phase (Fig. 6). The absence of ($00l$) peaks in the XRD patterns of the MWW-LDH-*in situ* samples suggests that the LDH sheets are irregularly stacked. This irregular stacking is likely the result of a limited number of LDH layers and significant disruption in their orderly arrangement. We hypothesize that this disruption arises from the interaction between the LDH sheets and the MWW sheets. The presence of MWW sheets likely interferes with the nucleation and growth of LDH layers, hindering their ability to stack in a regular, well-ordered fashion. As a result, the formation of disordered and sparsely stacked LDH sheets is observed, accounting for the absence of the ($00l$) peak in the XRD pattern. Thus, the interplay between MWW and LDH sheets plays a crucial role in determining the structural organization and stacking behaviour of LDH in these composite samples. It is noteworthy that after the calcination process, the expected diffraction bands corresponding to the metal oxides were not clearly detected, which is being associated with a homogeneous dispersion of MgAlCe oxides distributed evenly throughout the structural framework of the MCM-22 zeolite. Only in the sample with a higher amount of *in situ* formed MgAlCe hydrotalcite phase (MWW-LDH-*in situ*-50), it was possible to observe the presence of low intense diffraction bands characteristic of metal oxides from calcined LDH nanometric sub-domains (Fig. 6). This fact is corroborated by the results obtained through EDX-TEM, where a homogeneous distribution of Mg, Al, and Ce elements, due to metal oxide sub-domains, in the MWW zeolite crystals is observed, preserving their laminar arrangement and characteristic porosity (Fig. 2 and 7).

Chemical analysis of the MWW-LDH-*in situ* samples shows that the amounts of Mg, Al, and Ce increased in the final multi-component materials obtained due to the growing use of the respective inorganic salts for the *in situ* formation of LDH sub-domains located in the free inner volume of the MWW network (Table 1). In all cases, the Al/(Mg + Al + Ce) molar ratios characteristic of LDH phases, in the theoretical range of 0.20 – 0.33, were closely maintained in the final materials, confirming the formation of hydrotalcite-type phases in the obtained multi-component materials. Thermogravimetric analysis of the MWW-LDH-*in situ* samples formed using method (II) revealed that the solids exhibited a primary weight loss of around ~ 350 °C, which is associated with the characteristic thermal transformation from LDH phases to MgAlCe oxides due to the removal of anionic counter-ions used during the synthesis process. This weight loss was more pronounced when the amount of hydrotalcite counterparts is higher in the as-synthesized samples. In addition, a second weight loss at higher temperatures ($T > 500$ °C) was also observed, which is mainly assigned to dehydroxylation caused by the condensation of

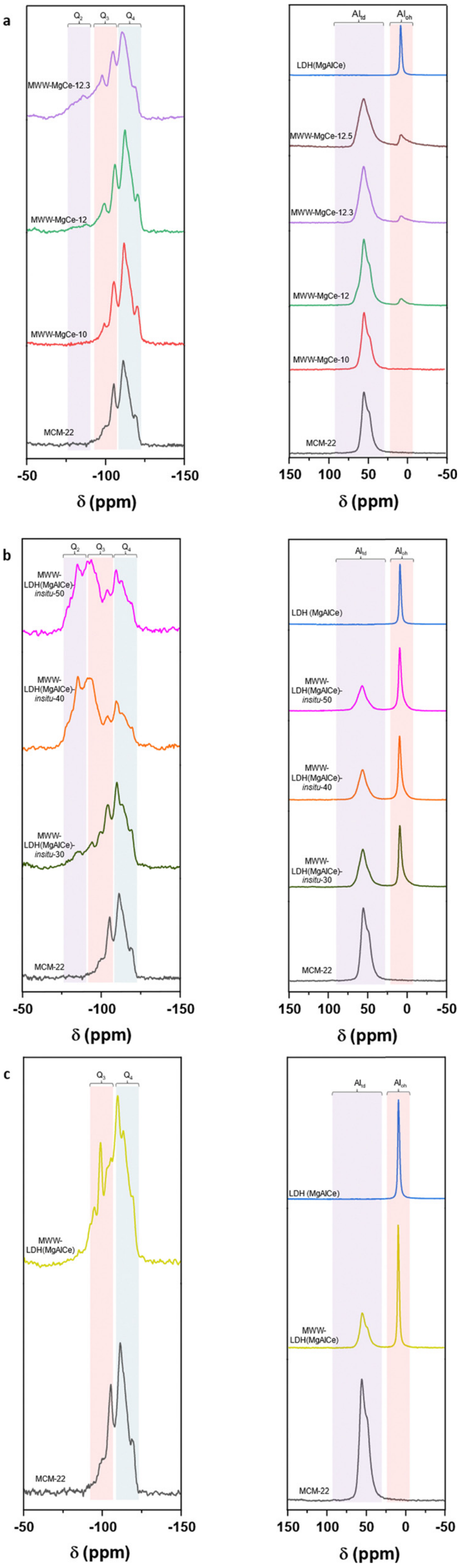

Fig. 3 ^{29}Si BD MAS NMR (left) and ^{27}Al MAS NMR (right) spectra. (a) As-synthesized multi-component MWW-MgCe materials obtained through method (I) at different pHs for the formation of metallic oxide sub-domains. (b) As-synthesized multi-component MWW-LHD-*in situ* materials obtained following synthesis method (II) with different LDH content. (c) As-synthesized multi-component MWW-LHD materials obtained following synthesis method (III).

external silanol groups present in the individual MWW layers, although the decarbonatation phenomenon could continue at high temperatures (Fig. S1 and S2, ESI†).

Through ^{29}Si NMR spectra, it is confirmed that the zeolitic structure is preserved overall due to the identification of all characteristic Q-type chemical shifts from the MWW zeolitic counterpart (Fig. 3). The alteration observed in the chemical shifts Q^2 and Q^3 identified in the MWW-LDH *in situ* materials is noteworthy, as they exhibit higher intensity and width than the pristine MWW precursor. This effect could be attributed to the presence of *in situ* formed hydrotalcite MgAlCe sub-domains interacting with external silanol groups located on the external surface of the individual MWW layers.[40] This result would corroborate the effective formation of LDH nanometric phases in the final materials, homogenously distributed in the zeolitic matrix and closely linked to silicoaluminate tetrahedral sites. On the other hand, ^{27}Al NMR spectra clearly show the presence of octahedral aluminium in the MWW-LDH-*in situ* materials, typical of MgAlCe hydrotalcites formed in the MWW-type structure that retains the characteristic tetrahedral aluminium positions (Fig. 3). From these results, it was possible to estimate that approximately 43–51% of total aluminium of the multi-component solids obtained were attributed to the *in situ* formed MgAlCe hydrotalcite-phase, and this content is greatly reduced (∼3%) when the materials were prepared through method (I) without using external aluminium sources for LDH generation in the MWW zeolitic matrix. These results would corroborate that these synthesis conditions of method (II) effectively favour the chemical modification of the MWW zeolitic layers, facilitating their chemical interaction with the *in situ* formed LDH sub-domains.

UV-vis spectroscopy clearly revealed a strong peak at ∼330 nm for the multi-component MWW-LDH-*in situ* materials associated with the presence of hydrotalcite-type sub-domains containing oxyhydroxide cerium species in the as-synthesized samples. This peak corresponds to the transitions where Ce 4f electrons are involved. This absorption peak was more prominent when the LDH content in the final materials was higher and was preserved after the calcination process, reflecting the generation of homogenously distributed CeO_2 at the nanometric scale in the free volume of the MWW zeolitic framework (Fig. S3, ESI†).

Similar to multi-component materials prepared through methodology (I), textural properties of MWW-LDH-*in situ* materials showed that the specific surface area and microporous contribution of the samples markedly decreased when the content of *in situ* MgAlCe formed phases was more significant, using external aluminium sources during the synthesis process. This result would be associated with the increased formation of homogeneously distributed metallic oxide sub-domains in the MWW framework, after the calcination step, which exhibited a more compact network and reduced internal porosity than lamellar MWW zeolitic matrixes (Table 2 and Fig. S4, ESI†). This effect was even more pronounced due to the partial blockage of free pore volume by the presence of metallic species located in zeolitic cavities and channels. However, the observed increase in the total volume of the samples when the presence

Table 2 Textural properties of the multi-component MWW-MgCe, MWW-LHD-*in situ* and MWW-LHD materials obtained following synthesis methods (I), (II) and (III), respectively, from N_2 adsorption isotherms

Sample	BET surface area ($m^2\ g^{-1}$)	*t*-plot micropore area ($m^2\ g^{-1}$)	*t*-plot micropore volume ($cm^3\ g^{-1}$)	V_{total} ($cm^3\ g^{-1}$)
MCM-22	487	408	0.162	0.490
LDH (MgAlCe)	139	12	0.004	0.346
MWW-MgCe materials				
MWW-MgCe-10	493	373	0.150	0.505
MWW-MgCe-12	344	166	0.070	0.570
MWW-MgCe-12.3	310	118	0.051	0.568
MWW-MgCe-12.5	279	42	0.020	0.599
MWW-LHD-*in situ* materials				
MWW-LDH(MgAlCe)-*in situ*-30	396	311	0.130	0.465
MWW-LDH(MgAlCe)-*in situ*-40	347	156	0.066	0.501
MWW-LDH(MgAlCe)-*in situ*-50	283	85	0.040	0.553
MWW-LHD materials				
MWW-LDH(MgAlCe)	327	180	0.074	0.432

of metallic oxide phases was more elevated should be associated with a smaller crystal size characteristic of calcined hydrotalcite phases and the generated interparticle volume between the formed metal oxide sub-domains.

In addition, calcined MWW-LDH-*in situ* solids exhibited H_2-TPR curves with reducibility signals mainly focused in the 300–400 °C range, with these peaks practically non-existent in the pristine MWW zeolitic support (Fig. 4). This signal was assigned to the reduction temperature of CeO_2 generated at high temperatures from MgAlCe phases formed *in situ* during the synthesis process. It is important to point out that this H_2 reduction peak significantly shifted at higher temperatures, close to 400 °C, when the LDH content present in the multi-component materials was higher, suggesting a higher likelihood of the formation of CeO_2 agglomerates.

From the TPD-ammonia spectrum, it was possible to identify one main band, centred at ∼300–350 °C, associated with the oxyhydroxy cerium phases derived from MgAlCe hydrotalcite phases treated at high temperatures. The broadness of this desorption signal, compared with the TPD curve of the pure LDH material, would be probably indicative of the homogenous distribution and strong interaction of MgAlCe sub-domains with the MWW zeolitic counterpart. This band was more intense when the amount of *in situ* formed hydrotalcite was higher in the final multi-component materials (Table S1 (ESI†) and Fig. 5). As with the samples obtained using method (I), two desorption bands centred at approximately 200 °C and 400 °C, associated with the acid centres of the MWW zeolite present in the multi-component materials, were also observed.

3.3. Method (III): Synthesis of MWW-LDH materials

The third route for the preparation of multicomponent materials (III) was based on a swelling and subsequent intercalation process of the laminar precursor of the MWW-type zeolite in order to incorporate sub-domains of MgAlCe hydrotalcite, previously prepared, into the interlamellar space as intercalation units, separating the zeolite layers from each other (MWW-LDH) (Scheme 1). Through this methodology, it would be possible to incorporate in the zeolitic matrix well-formed LDH MgAlCe phases distributed like bigger agglomerates located between the individual MWW layers. Indeed, the successful intercalation of LDH domains within the MWW layers would likely be facilitated by electrostatic interactions between the negatively charged silicate layers of the MWW zeolite and the positively charged hydroxide layers of the preformed LDH phases. This electrostatic attraction should help stabilize the LDH sub-domains in the interlayer spaces, promoting a uniform distribution of active sites within the material. To achieve this, an initial stage of swelling of the laminar MWW zeolite precursor was carried out using long-chain surfactants ($CTMA^+OH^-/Br^-$), which through cation exchange, facilitated the controlled separation of individual zeolitic layers. In the second stage, an intercalation process was carried out using previously prepared MgAlCe hydrotalcite with an Al/(Mg + Al + Ce) ratio of ∼0.21 [27]. The results obtained through X-ray diffraction show that the LDH phase is clearly present in the final material, cohabitating with the MWW zeolite, and all characteristic diffraction bands of the MgAlCe hydrotalcite can be detected, including the more prominent ones located at ∼11°, ∼22° and ∼33° 2θ, corresponding to the (h00) layered LDH planes (Fig. 8). In addition, XRD measurements revealed a slight increase in the interlayer distance following LDH intercalation. This expansion likely results from the insertion of LDH subdomains between the MWW layers, supporting the presence of intercalated species within the structure. After a calcination process, the diffraction patterns obtained revealed the formation of MgAl oxides together with the detection of fluorite (CeO_2), characteristic of MgAlCe-type LDHs subjected to high temperature processes. In addition, from TEM micrographs, it was confirmed that the lamellar morphology of the MWW-type zeolitic framework was preserved after the intercalation process with hydrotalcite phases, with distinguished well-structured and superposed zeolitic sheets (Fig. 2). Chemical analysis determined that the initial Al/(Mg + Al + Ce) molar ratio present in the used hydrotalcite was maintained after the synthesis process (Table 1). Furthermore, the Si/Al ratio of the MWW zeolite precursor was 15,

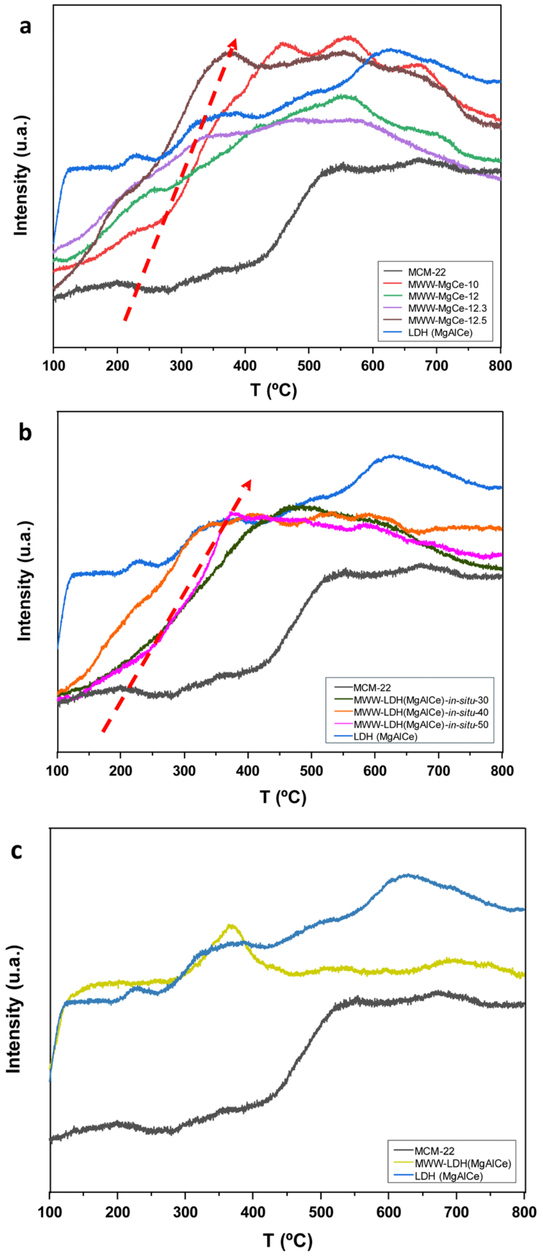

Fig. 4 H_2 thermoprogrammed reduction (TPR) curves. (a) Multi-component MWW-MgCe materials obtained through method (I) at different pHs for the formation of metallic oxide sub-domains. (b) Multi-component MWW-LHD-*in situ* materials obtained following synthesis method (II) with different LDH content. (c) Multi-component MWW-LHD materials obtained following synthesis method (III).

which reduced during the incorporation of LDH intercalation units due to the presence of oxyhydroxyde MgAl species in the final MWW-LDH materials. Thermogravimetric analysis showed that these multi-component materials exhibited two main weight losses at 200 °C and 350 °C, associated with the degradation of surfactant molecules ($CTMA^{+}OH^{-}/Br^{-}$) and the transformation of MgAlCe hydrotalcite to metal oxides, respectively, used as swelling and intercalation agents during the preparation through methodology (III) (Fig. S1 and S2, ESI†).

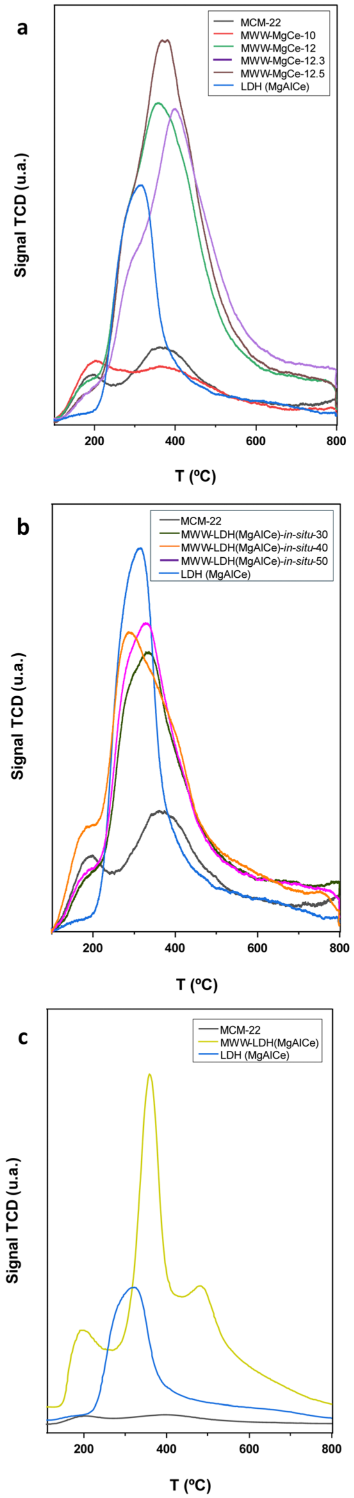

Fig. 5 NH_3 thermoprogrammed desorption (TPD) curves. (a) Multi-component MWW-MgCe materials obtained through method (I) at different pHs for the formation of metallic oxide sub-domains. (b) Multi-component MWW-*in situ* materials obtained through method (II) with different LDH content. (c) Multi-component MWW-LDH materials (right) obtained through method (III).

The results obtained through ^{29}Si and ^{29}Al NMR spectroscopy confirmed the presence of octahedral and tetrahedral

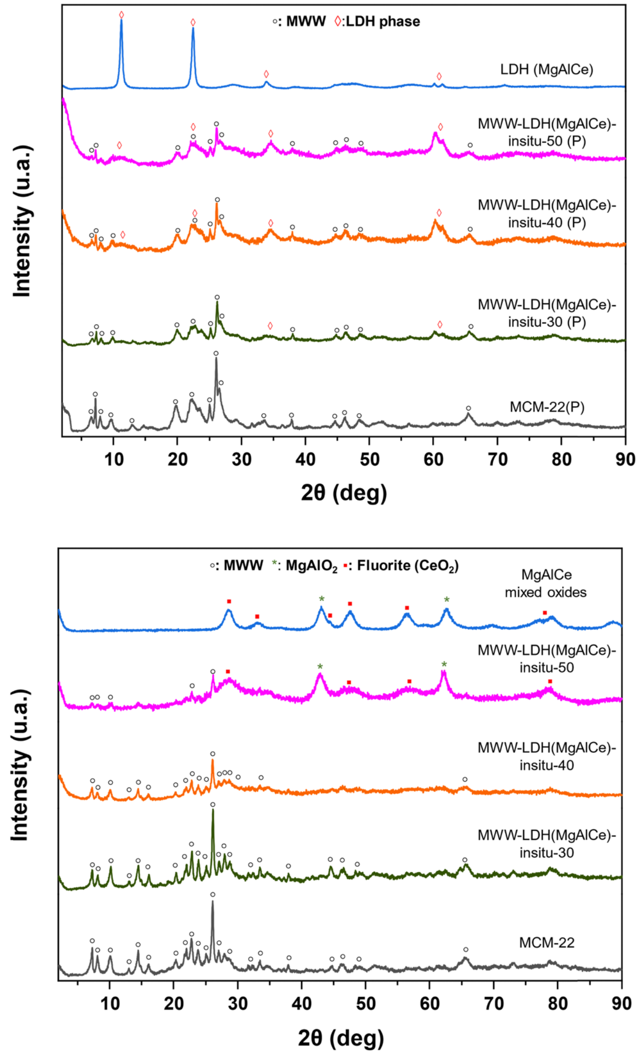

Fig. 6 XRD patterns of the multi-component MWW-LHD-*in situ* materials obtained following synthesis method (II): (top) as-synthesized samples; (bottom) calcined samples.

aluminium from the MgAlCe hydrotalcite and the MWW zeolitic counterpart, respectively, as well as the presence of Q^3 and Q^4 silicon atoms characteristic of MWW zeolite structures, once again confirming the preservation of the MWW structural framework after the generation of the MWW-LDH materials through the swelling and intercalation method (Fig. 3). The data obtained through UV-vis showed the effective presence of CeO_2 species, in the multi-component solids, with the characteristic absorption band located at 330 nm, associated with 4f electron transitions (Fig. S3, ESI†). From the N_2 adsorption isotherms, it was observed that the intercalation of MgAlCe sub-domains, located between MWW individual zeolitic layers, resulted in a strong decrease in the specific surface area and free porous volume of the multi-component MWW-LDH materials. This fact is probably associated with the partial blockage of the porosity for the metal oxide counterparts located in the interlamellar space, covering the external surface of the MWW layers and closing the entrance to the internal zeolitic channels (Table 2 and Fig. S4, ESI†). The presence of ceria species in the multi-component MWW-LDH materials was also confirmed from H_2-TPR curves where main reducibility signal focused at approximately 370 °C was detected, which is attributed to the reduction temperature of CeO_2 aggregates formed from MgAlCe hydrotalcite phase treated through high thermal processes and located in the interlayer zeolitic space, forming part of the intercalated metal oxide units (Fig. 4). From the TPD study, it was possible to identify intense ammonia desorption bands at ~200 °C and ~400 °C associated with the presence of acid sites, derived from surface silanol groups and tetrahedral aluminium, located in the zeolitic counterpart of the multi-component MWW-LDH materials. In addition, one desorption band was also observed at ~300–350 °C mainly due to the cerium oxide species from the MgAlCe hydrotalcite counterpart, generated after the thermal process, and located between the individual MWW layers (Table S1 (ESI†) and Fig. 5). In this case, the detection of the different acid sites, from both components, was clearly identified separately, suggesting that the chemical interaction between the zeolitic and metal oxide sub-domains was less pronounced, compared with the samples obtained from methods (I) and (II), as detailed above, where overlapping in the desorption bands was detected. Thus, the results obtained analysing the characterization data of the multi-component MWW-LDH materials obtained through method (III), after swelling and intercalation steps, confirmed that both the hydrotalcite and zeolitic phases retained their physico–chemical characteristic after the preparation process.

3.4. Comparative discussion

This work successfully demonstrated the preparation of multi-component materials containing zeolitic MWW layers and sub-domains of mixed metal and/or metal oxides following different synthesis strategies. The results revealed that the multi-component materials prepared through the three approaches exhibited remarkably different structural properties.

The methods (I) and (II) involved the attempted *in situ* formation of MgAlCe hydrotalcite phases, while method (III) utilized a multi-step swelling and intercalation process with LDH phase previously formed in the presence of the MWW lamellar precursor. After calcination, all three approaches successfully yielded multi-component materials comprising zeolitic layers and Mg/Al/Ce oxides and/or mixed oxide species. In any case, significant differences were observed between the methodologies used. Indeed, when attempting to prepare an *in situ* LDH phase using the MWW-type zeolitic matrix as an aluminium source for hydrotalcite formation, the content of the deposited mixed oxides was low. Predominantly, MgAl oxyhydroxides and CeO_2 nanoparticles were homogeneously distributed on the surface of the zeolitic layers and within their free porous volume (method I), even under optimal pH conditions for *in situ* LDH formation. Enhanced interactions between the MgAlCe hydrotalcite sub-domains and the MWW-type zeolitic layers were achieved when an additional external aluminium source was introduced during the synthesis process for the *in situ* LDH phase formation (method II). This led to the

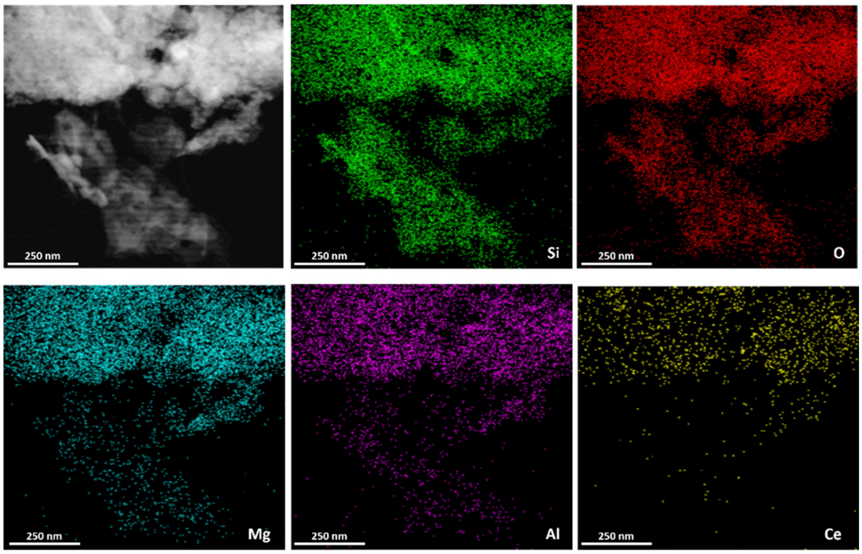

Fig. 7 TEM-EDX mapping analysis of the multi-component MWW-LHD-*in situ*-50 sample obtained following synthesis method (II).

successful incorporation of larger amounts of MgAlCe hydrotalcite phases, which interacted directly at the nanoscale with the zeolitic framework, as evidenced by the changes in the chemical environment of the tetrahedral siliceous units of the MWW-type structure. Notably, no CeO_2 nanoparticle aggregates were observed, as seen in method (I). Finally, when preformed MgAlCe hydrotalcites were used as intercalation agents, both components were clearly present in the final material. However, larger LDH sub-domains were observed in the interlamellar space than in the previous cases, with weaker nanoscale interactions with the zeolitic matrix, acting as intercalation units located between MWW layers. Overall, the characterization studies confirmed the effective formation of multi-component solid materials, generated by the successful combination of MgAlCe hydrotalcite and/or metal oxide sub-domains and the laminar MWW zeolite. This integration promoted the presence of various accessible Lewis and Brönsted acidic and basic sites within a single heterogeneous material, enhancing its use as a potential multi-functional catalyst, where such active sites would act cooperatively. In addition, the band gap values estimated for the multi-component materials, particularly the MWW-MgCe series with a band gap as low as ~2.45 eV, suggest that these materials may exhibit photoresponsive properties suitable for photocatalytic applications (Fig. S3 and Table S2, ESI†). This range of band gaps would indicate potential activation under visible light, which could make these multi-component materials candidates for redox-driven photocatalytic processes.

Interestingly, the location and interaction of oxide subdomains within the MWW layers affect the reducibility of CeO_2 and the acid-basic properties across the three series of materials, which is crucial for understanding the catalytic potential of each material type. In our study, the reducibility of CeO_2 and the acid-basic profile were indeed influenced by the method of subdomain incorporation. For instance, H_2-TPR profiles showed that CeO_2 reduction peak temperatures were lower in MWW-MgCe samples than in those prepared by the MWW-LDH-*in situ* and MWW-LDH intercalation methods (Fig. 4). This behaviour suggests a stronger interaction between CeO_2 nanoparticles and the MWW layers in the MWW-MgCe series. This is likely due to the close contact achieved during *in situ* formation, which facilitates the reduction of CeO_2 at lower temperatures. Conversely, in the MWW-LDH intercalated samples, the reduction peak for CeO_2 shifted to higher temperatures, indicating weaker interaction, as the larger, more isolated LDH subdomains in the interlayer spaces reduce less readily.

Furthermore, the NH_3-TPD results reveal varied acid site strengths across the samples, which correlate with the integration approach of the MgAlCe phases. MWW-MgCe samples show a progressive increase in ammonia desorption with pH, with the highest desorption observed in MWW-MgCe-12.5. This trend suggests a higher density of accessible acid sites in samples synthesized at elevated pH, where oxide subdomains are more pronounced. In comparison, MWW-LDH-*in situ* samples exhibit moderate ammonia desorption values, indicating that while LDH phases are present, their integration within the MWW matrix may limit direct acid site accessibility. The intercalated MWW-LDH samples present a distinct desorption behaviour, reflecting more isolated acid sites within interlamellar spaces (Fig. 5 and Table S1, ESI†).

This comparative analysis highlights that MWW-MgCe materials, with their higher density of accessible acid sites, may be more suited for reactions requiring robust acid-basic functionality, while MWW-LDH-*in situ* and MWW-LDH samples may favour applications with moderate acid requirements due to the restricted accessibility of acid sites.

Thus, the development of such advanced multi-functional solid catalysts is crucial for advancing sustainable catalytic processes and supporting the transition towards a circular economy and chemistry, and reducing dependence on fossil

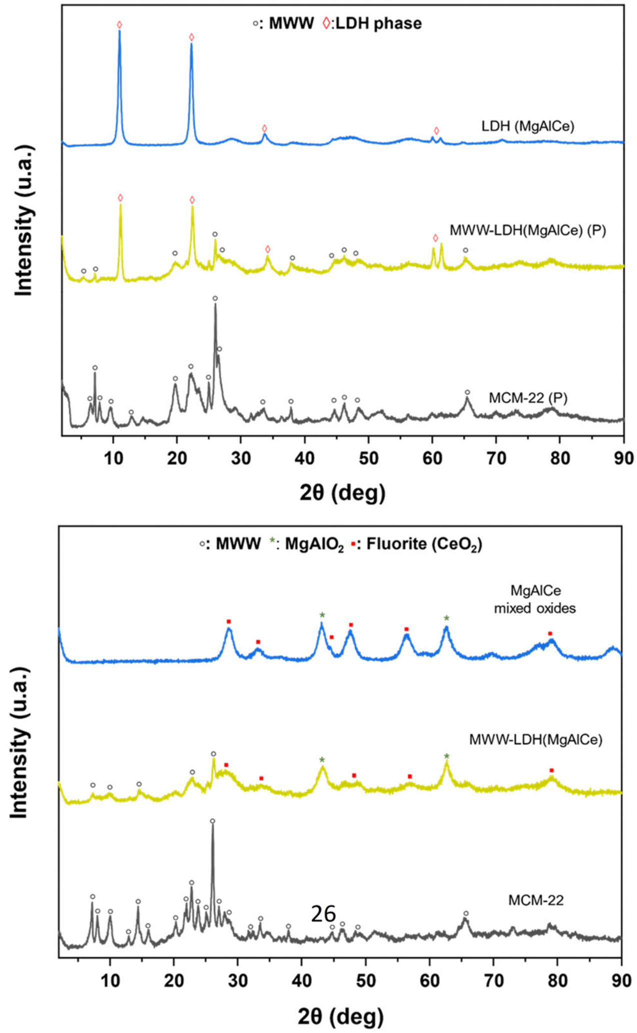

Fig. 8 XRD patterns of the multi-component MWW-LHD materials obtained following synthesis method (III): (top) as-synthesized samples; (bottom) calcined samples.

sources. Given the versatility of both zeolites and hydrotalcites, we will continue to work on exploring their tuneable properties, such as their customizable composition, adjustable particle morphology and porous architecture/structure, robustness, efficiency and recyclability to produce a variety of multi-component materials in which different active sites act cooperatively to produce clean energy and sustainable chemicals and fine chemicals.

4. Conclusions

In this study, we successfully prepared three families of multi-component materials by integrating MWW-type zeolitic layers with MgAlCe oxide sub-domains at the nanoscale, using three distinct synthetic routes. Methods (I) and (II) involved the co-precipitation of MgAlCe oxide and hydroxide in the presence of MWW zeolites, while method (III) employed swelling and intercalation of MWW layers with pre-formed LDH phases. After calcination, these approaches yielded multi-component materials with zeolitic layers and MgAlCe oxides that displayed notable structural differences, resulting in varied metallic active sites which influenced their catalytic behaviours. We are currently studying their catalytic performance in oxidation reactions *via* the Baeyer–Villiger mechanism, as well as in isomerization, hydrogenation, and water-splitting processes. The tuneable composition of the zeolite and LDH components, along with the adjustable porous architecture, offers unique opportunities for catalytic optimization. The development of such tailored, high-activity multi-component catalysts represents a significant step forward in promoting sustainable catalytic processes and contributing to a healthier planet.

Author contributions

C. E.: investigation, data curation, formal analysis, methodology, visualization, and writing – original draft; A. V.: conceptualization, data curation, validation, project administration, supervision, and writing – review & editing; U. D.: conceptualization, data curation, validation, funding acquisition, project administration, supervision, and writing – review & editing.

Data availability

The data supporting this article have been included as part of the ESI.†

Conflicts of interest

There are no conflicts to declare.

Acknowledgements

The authors are grateful for the financial support from the Spanish Ministry (projects PID2020-112590GB-C21, PID2023-146114NB-C21 and CEX2021-001230-S, funded by MCIN/AEI/10.13039/501100011033). This study forms part of the Advanced Materials program and was supported by MCIN with funding from the European Union NextGeneration (PRTR-C17.I1) and by Generalitat Valenciana (MFA/2022/003). C. E. has been partially supported by the Spanish Government through the FPI pre-doctoral scholarship number PRE2019-089547 under project SEV-2016-0683-19-3.

References

1 J. Bao, G. Yang, Y. Yoneyama and N. Tsubaki, Significant Advances in C1 Catalysis: Highly Efficient Catalysts and Catalytic Reactions, *ACS Catal.*, 2019, **9**(4), 3026–3053, DOI: **10.1021/acscatal.8b03924**.

2 A. Velty and A. Corma, Advanced zeolite and ordered mesoporous silica-based catalysts for the conversion of CO2 to chemicals and fuels, *Chem. Soc. Rev.*, 2023, **52**(5), 1773–1946, DOI: **10.1039/d2cs00456a**.

3 A. S. Mahadevi and G. N. Sastry, Cooperativity in Noncovalent Interactions, *Chem. Rev.*, 2016, **116**(5), 2775–2825, DOI: **10.1021/cr500344e**.

4 T. Chen, M. Qiu, Y. Peng, C. Yi and Z. Xu, Engineering synergistic effects of immobilized cooperative catalysts, *Coord. Chem. Rev.*, 2023, **474**, 214863, DOI: **10.1016/j.ccr.2022.214863**.

5 U. Díaz and A. Corma, Organic-Inorganic Hybrid Materials: Multi-Functional Solids for Multi-Step Reaction Processes, *Chem. Eur. J.*, 2018, **24**(16), 3944–3958, DOI: **10.1002/chem.201704185**.

6 B. Li, M. Chrzanowski, Y. Zhang and S. Ma, Applications of metal-organic frameworks featuring multi-functional sites, *Coord. Chem. Rev.*, 2016, **307**, 106–129, DOI: **10.1016/j.ccr.2015.05.005**.

7 Y.-M. Wang, G.-H. Ning and D. Li, Multifunctional Metal-Organic Frameworks as Catalysts for Tandem Reactions, *Chem. – Eur. J.*, 2024, **30**(26), e202400360, DOI: **10.1002/chem.202400360**.

8 U. Díaz, Layered Materials with Catalytic Applications: Pillared and Delaminated Zeolites from MWW Precursors, *ISRN Chem. Eng.*, 2012, Article ID 537164, DOI: **10.5402/2012/537164**.

9 W. J. Roth, B. Gil, W. Makowski, B. Marszaleka and P. Eliasova, Layer like porous materials with hierarchical structure, *Chem. Soc. Rev.*, 2016, **45**(12), 3400–3438, DOI: **10.1039/c5cs00508f**.

10 A. Corma, V. Fornés, S. B. Pergher, T. L. M. Maesen and J. G. Buglass, Delaminated zeolite precursors as selective acidic catalysts, *Nature*, 1998, **396**(6709), 353–356, DOI: **10.1038/24592**.

11 J. O. Barth, J. Kornatowski and J. A. Lercher, Synthesis of new MCM-36 derivatives pillared with alumina or magnesia alumina, *J. Mater. Chem.*, 2002, **12**(2), 369–373, DOI: **10.1039/B104824B**.

12 U. Díaz, D. Brunel and A. Corma, Catalysis using multifunctional organosiliceous hybrid materials, *Chem. Soc. Rev.*, 2013, **42**(9), 4083–4097, DOI: **10.1039/c2cs35385g**.

13 K. Wang, K. N. Hui, K. S. Hui, S. Peng and Y. Xu, Recent progress in metal–organic framework/graphene-derived materials for energy storage and conversion: design, preparation, and application, *Chem. Sci.*, 2021, **12**(16), 5737–5766, DOI: **10.1039/D1SC00095K**.

14 A. Corma, U. Díaz, T. García, G. Sastre and A. Velty, Multifunctional Hybrid Organic−Inorganic Catalytic Materials with a Hierarchical System of Well-Defined Micro- and Mesopores, *J. Am. Chem. Soc.*, 2010, **132**(42), 15011–15021, DOI: **10.1021/ja106272z**.

15 D. Chaillot, S. Bennici and J. Brendlé, Layered double hydroxides and LDH-derived materials in chosen environmental applications: a review, *Environ. Sci. Pollut. Res.*, 2021, **28**, 24375–24405, DOI: **10.1007/s11356-020-08498-6**.

16 S. M. Humphrey, P. K. Allan, S. E. Oungoulian, M. S. Ironsidea and E. R. Wisea, Metal–organophosphine and metal–organophosphonium frameworks with layered honeycomb-like structures, *Dalton Trans.*, 2009, 2298–2305, DOI: **10.1039/b820038f**.

17 L. Feng, K.-Y. Wang, G. S. Daya and H.-C. Zhou, The chemistry of multi-component and hierarchical framework compounds, *Chem. Soc. Rev.*, 2019, **48**(18), 4823–4853, DOI: **10.1039/c9cs00250b**.

18 X.-Z. Xie, L. Xu, Y. Pan and J.-X. Mi, Facile synthesis of rose-like composites of zeolites and layered double hydroxides: Growth mechanism and enhanced properties, *Chemosphere*, 2022, **309**, 136741, DOI: **10.1016/j.chemosphere.2022.136741**.

19 T. Baskaran, J. Christopher, M. Mariyaselvakumar and A. Sakthivel, Preparation of an MCM 22/Hydrotalcite Framework Composite and Its Catalytic Application, *Eur. J. Inorg. Chem.*, 2017, 2396–2405, DOI: **10.1002/ejic.201601398**.

20 W. J. Roth, M. Opanasenko, M. Mazur, B. Gil, J. Cejka and T. Sasaki, Current State and Perspectives of Exfoliated Zeolites, *Adv. Mater.*, 2024, **36**(4), 2307341, DOI: **10.1002/adma.202307341**.

21 A. Kuschel, M. Drescher, T. Kuschel and S. Polarz, Bifunctional Mesoporous Organosilica Materials and Their Application in Catalysis: Cooperative Effects or Not, *Chem. Mater.*, 2010, **22**(4), 1472–1482, DOI: **10.1021/cm903412e**.

22 W. J. Roth and J. Cejka, Two-dimensional zeolites: dream or reality?, *Catal. Sci. Technol.*, 2011, **1**, 43–53, DOI: **10.1039/C0CY00027B**.

23 A. P. Tathod, B. Saini, S. Arumugam and N. Viswanadham, Hybrid Nanocomposite Comprising Mg−Al Hydrotalcite Nanocrystals on ZSM-5 Zeolite for Production of Renewable Fuel Additives from Furfural, *ACS Appl. Nano Mater.*, 2023, **6**(5), 3580–3589, DOI: **10.1021/acsanm.2c05349**.

24 A. Corma, U. Díaz, V. Fornés, J. M. Guil, J. Martínez-Triguero and E. J. Creyghton, Characterization and catalytic activity of MCM-22 and MCM-56 compared with ITQ-2, *J. Catal.*, 2000, **191**(1), 218–224, DOI: **10.1006/jcat.1999.2774**.

25 X. Liu and Z. Zhu, Synthesis and Catalytic Applications of Advanced Sn- and Zr-Zeolites Materials, *Adv. Sci.*, 2024, **11**(11), 2306533, DOI: **10.1002/advs.202306533**.

26 Z. Zhu, Hao Xu, J. Jiang, Y. Guan and Peng Wu, Sn-Beta zeolite hydrothermally synthesized via interzeolite transformation as efficient Lewis acid catalyst, *J. Catal.*, 2017, **352**, 1–12, DOI: **10.1016/j.jcat.2017.04.031**.

27 M. J. Climent, A. Corma, S. Iborra, K. Epping and A. Velty, Increasing the basicity and catalytic activity of hydrotalcites by different synthesis procedures, *J. Catal.*, 2004, **225**, 316–326, DOI: **10.1016/j.jcat.2004.04.027**.

28 Z. Wang, W. Zhang, C. Li and C. Zhang, Recent Progress of Hydrogenation and Hydrogenolysis Catalysts Derived from Layered Double Hydroxides, *Catalysts*, 2022, **12**(11), 1484, DOI: **10.3390/catal12111484**.

29 G. Li, E. A. Pidko and E. J. M. Hensen, Synergy between Lewis acid sites and hydroxyl groups for the isomerization of glucose to fructose over Sn-containing zeolites: a theoretical perspective, *Catal. Sci. Technol.*, 2014, **4**(8), 2241–2250, DOI: **10.1039/C4CY00186A**.

30 M. Puche-Panadero and A. Velty, Readily available Ti-beta as an efficient catalyst for greener and sustainable production of campholenic aldehyde, *Catal. Sci. Technol.*, 2019, **9**(16), 4293–4303, DOI: **10.1039/C9CY00957D**.

31 S. Dai, E. Montero-Lanzuela, A. Tissot, H. G. Baldoví, H. García, S. Navalón and C. Serre, Room temperature design of Ce(IV)-MOFs: from photocatalytic HER and OER to overall water splitting under simulated sunlight irradiation, *Chem. Sci.*, 2023, **14**(13), 3451–3461, DOI: 10.1039/D2SC05161C.

32 A. Corma, C. Corell and J. Pérez-Pariente, Synthesis and characterization of theMCM-22 zeolite, *Zeolites*, 1995, **15**(1), 2–8, DOI: 10.1016/0144-2449(94)00013-I.

33 M. E. Leonowicz, J. A. Lawton, S. L. Lawton and M. K. Rubin, MCM-22: A Molecular Sieve with Two Independent Multidimensional Channel Systems, *Science*, 1994, **264**(5167), 1910–1913, DOI: 10.1126/science.264.5167.1910.

34 H. Guo, L. Tang, K. Li, P. Ning, J. Peng, F. Lu, J. Gu, S. Bao, Y. Liu, T. Zhu and Z. Duan, Influence of the preparation conditions of MgAlCe catalysts on the catalytic hydrolysis of carbonyl sulfide at low temperature, *RSC Adv.*, 2015, **5**(26), 20530–20537, DOI: 10.1039/c5ra00463b.

35 P. Sinha, A. Datar, C. Jeong, X. Deng, Y. G. Chung and L.-C. Lin, Surface Area Determination of Porous Materials Using the Brunauer–Emmett–Teller (BET) Method: Limitations and Improvements, *J. Phys. Chem. C*, 2019, **123**(33), 20195–20209, DOI: 10.1021/acs.jpcc.9b02116.

36 J. Calvache-Muñoz, F. A. Prado and J. E. Rodríguez-Páez, Cerium oxide nanoparticles: Synthesis, characterization and tentative mechanism of particle formation, *Colloids Surf., A*, 2017, **529**, 146–159, DOI: 10.1016/j.colsurfa.2017.05.059.

37 B. Jiang, Z. Xi, F. Lu, Z. Huang, Y. Yang, J. Sun, Z. Liao, J. Wang and Y. Yang, Ce/MgAl mixed oxides derived from hydrotalcite LDH precursors as highly efficient catalysts for ketonization of carboxylic acid, *Catal. Sci. Technol.*, 2019, **9**(22), 6335, DOI: 10.1039/c9cy01323g.

38 S. Watanabe, X. Ma and C. Song, Characterization of Structural and Surface Properties of Nanocrystalline TiO_2-CeO_2 Mixed Oxides by XRD, XPS, TPR, and TPD, *J. Phys. Chem. C*, 2009, **113**(32), 14249–14257, DOI: 10.1021/jp8110309.

39 A. Lacarriere, F. Luck, D. Swierczynski, F. Fajula and V. Hulea, Methanol to hydrocarbons over zeolites with MWW topology: Effect of zeolite texture and acidity, *Appl. Catal., A*, 2011, **402**(1–2), 208–217, DOI: 10.1016/j.apcata.2011.06.003.

40 D. H. Brouwer, *Applications of silicon-29 NMR spectroscopy, Comprehensive Inorganic Chemistry III*, Elsevier Ltd., 2023, vol. 9, pp. 107–136, DOI: 10.1016/B978-0-12-823144-9.00032-7.